

# Rescaling of metal oxide nanocrystals for energy storage having high capacitance and energy density with robust cycle life

Hyung Mo Jeong<sup>a</sup>, Kyung Min Choi<sup>a</sup>, Tao Cheng<sup>b</sup>, Dong Ki Lee<sup>a</sup>, Renjia Zhou<sup>c</sup>, Il Woo Ock<sup>d</sup>, Delia J. Milliron<sup>c,e</sup>, William A. Goddard III<sup>b,1</sup>, and Jeung Ku Kang<sup>a,d,1</sup>

<sup>a</sup>Department of Materials Science and Engineering, Korea Advanced Institute of Science and Technology, Daejeon 305-701, Republic of Korea; <sup>b</sup>Materials and Process Simulation Center, California Institute of Technology, Pasadena, CA 91125; <sup>c</sup>Molecular Foundry, Lawrence Berkeley National Laboratory, Berkeley, CA 94720; <sup>d</sup>Graduate School of Energy, Environment, Water and Sustainability, Korea Advanced Institute of Science and Technology, Daejeon 305-701, Republic of Korea; and <sup>e</sup>Department of Chemical Engineering, University of Texas at Austin, Austin, TX 78712

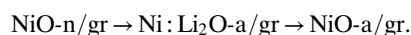
Contributed by William A. Goddard III, May 20, 2015 (sent for review December 9, 2014)

**Nanocrystals are promising structures, but they are too large for achieving maximum energy storage performance. We show that rescaling 3-nm particles through lithiation followed by delithiation leads to high-performance energy storage by realizing high capacitance close to the theoretical capacitance available via ion-to-atom redox reactions. Reactive force-field (ReaxFF) molecular dynamics simulations support the conclusion that Li atoms react with nickel oxide nanocrystals (NiO-n) to form lithiated core-shell structures (Ni:Li<sub>2</sub>O), whereas subsequent delithiation causes Ni:Li<sub>2</sub>O to form atomic clusters of NiO-a. This is consistent with in situ X-ray photoelectron and optical spectroscopy results showing that Ni<sup>2+</sup> of the nanocrystal changes during lithiation-delithiation through Ni<sup>0</sup> and back to Ni<sup>2+</sup>. These processes are also demonstrated to provide a generic route to rescale another metal oxide. Furthermore, assembling NiO-a into the positive electrode of an asymmetric device enables extraction of full capacitance for a counter negative electrode, giving high energy density in addition to robust capacitance retention over 100,000 cycles.**

rescaled atomic clusters | metal oxide nanocrystals | energy storage | molecular dynamic simulation | in situ electrochemical spectroscopy

The most critical challenge in energy storage is maximizing capacitance along with high power density and long cycle life. High-power capacitors (1–4) are candidates to meet this challenge, and can be classified into two categories: (i) energy storage systems where charge is stored in electrochemical double layers (EDLs) (5, 6) and (ii) pseudocapacitors that store charge by redox reactions (7–14). Unfortunately, EDLs have low capacitance, whereas metal oxide pseudocapacitors lead to short cycle life. Furthermore, typical capacitors have low energy density (5, 10). In principle, the capacitances of metal oxide crystals can be fully obtained via ion-by-atom surface redox reactions. A capacitor that enables high capacitance with high energy density and long cycle life thus would represent a major breakthrough in energy storage.

We synthesized metal oxide nanocrystals at a size of several nanometers on graphene, but found that rapid charging–discharging achieves only about 15% of their full capacitance. We hypothesized that reducing their sizes to the atomic clusters of subnanometer scales less than 1 nm, combined with conducting flexible graphene, would allow full redox reactions over entire constituents. Here we report that lithiation of 3-nm nickel oxide nanocrystals on graphene (NiO-n/gr) causes them to rescale down to subnanometer-scale Ni:Li<sub>2</sub>O-a/gr core-shell clusters and that subsequent delithiation of Ni:Li<sub>2</sub>O core-shell clusters leads to NiO (NiO-a/gr). We established the sequence as follows:



We then verified this using a combination of experimental characterization with complementary reactive molecular dynamics.

Moreover, we show that loading a positive electrode with NiO-a particles into an asymmetric full cell enables full capacitance of the counter negative electrode (15).

## Results and Discussion

We prepared NiO-n/gr as described in *SI Appendix, section S1*. The structure and the composition of NiO-n/gr were determined using transmission electron microscopy (TEM) and powder X-ray diffraction (*SI Appendix, Figs. S1 and S2*) showing size of ~3 nm. Next, the sample was combined with PVDF as a binder in an *N*-methyl-2-pyrrolidone (NMP) solution before the cell assembly. The cell was assembled with a 25-μm monolayer polypropylene membrane, followed by soaking in a 1 M LiPF<sub>6</sub> electrolyte solution with a mixture of ethylene carbonate (EC) and diethyl carbonate (DEC) (*Materials and Methods and SI Appendix, section S3*).

To rescale the NiO-n (Fig. 1*A*), we configured a cell with a lithium metal counter/reference electrode and carried out a cyclic voltammetry experiment using a VSP potentiostat (Bio-Logic) at a scan rate of 0.1 mV s<sup>−1</sup> (*SI Appendix, Fig. S3*). After the first cycle of lithiation and delithiation, we disassembled the cell and recovered NiO-a/gr and then washed the cell with acetone. Finally, we dried the NiO-a/gr in a vacuum oven. Next, we used dark-field scanning TEM (STEM) to demonstrate that this lithiation–delithiation process rescales NiO-n/gr to NiO-a/gr (Fig. 1*B* and *C*).

Using ex situ TEM, we traced the morphology of a single 3-nm NiO evolving during the rescaling process (Fig. 1*D* and *E* and

## Significance

The combined study of experiments and molecular dynamics simulations demonstrates that metal oxide nanocrystals on graphene can be rescaled into atomic clusters. It is notable that the capacitance of 3,023 F per the mass of NiO, matching the measured capacitance of 2,231 per the total electrode mass, exceeds the theoretical gravimetric capacitance of 2,618 F available via ion-to-atom redox reactions. This approach thus provides a new pathway to realize full capacitance via ion-to-atom Faradaic redox reactions. Furthermore, assembly with a rescaled metal oxide positive electrode shows that further development of high-capacity negative counter electrode materials can pave a new route to address challenging energy storage issues.

Author contributions: H.M.J. and J.K.K. designed research; H.M.J., K.M.C., R.Z., I.W.O., and J.K.K. performed research; D.K.L. and I.W.O. contributed new reagents/analytic tools; T.C. and W.A.G. analyzed data; and H.M.J., K.M.C., T.C., D.J.M., W.A.G., and J.K.K. wrote the paper.

The authors declare no conflict of interest.

<sup>1</sup>To whom correspondence may be addressed. Email: wag@wag.caltech.edu or jeung@kaist.ac.kr.

This article contains supporting information online at [www.pnas.org/lookup/suppl/doi:10.1073/pnas.1503546112/-DCSupplemental](http://www.pnas.org/lookup/suppl/doi:10.1073/pnas.1503546112/-DCSupplemental).





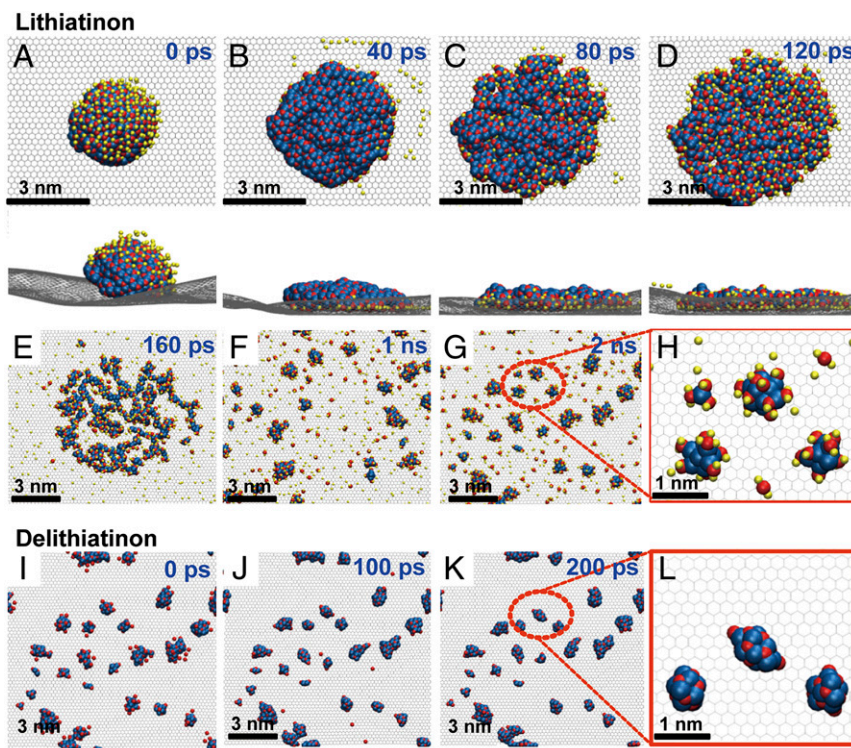


**Fig. 2.** ReaxFF molecular dynamics simulation of rescaling a 3-nm NiO nanoparticle during lithiation and delithiation at 298 K. (A) The simulation started from an equilibrated NiO semisphere placed on graphene with the addition of Li (23%) to all available surface O sites (view from top and side). A 40-ps NVT simulation was carried out with an external electronic field of  $0.03 \text{ V nm}^{-1}$ . The newly added Li experienced an additional  $3\text{-V nm}^{-1}$  electronic field, which could accelerate the diffusion of Li. (B) The obtained structure after the 40-ps MD simulation. More Li atoms (49%) were then added to the newly created surface O sites, and the same simulations were repeated for another two rounds. (C and D) The structures after an NVT simulation of these second and third round Li additions, respectively, where 848 Li atoms (100%) were added into the system after three rounds of Li addition. (E–G) The simulation was then extended to 2 ns and snapshots during the simulation are shown. (H) The enlargement of a selected area of G (red slashed rectangle) is shown in which the Ni–O–Li core shell structure can be clearly observed. (I–K) After removing all of the Li, a 200-ps NVT simulation was carried out to investigate the delithiation process. Snapshots taken during the simulation are also shown. (L) An enlargement of a selected area of K (red slashed rectangle) in which O reoxidized the Ni to form NiO at a subnanosized scale. Atoms are distinguished by different colors: C in gray, Ni in blue, O in red, and Li in yellow.

the atomic charge distributions on Ni in NiO (cap), Ni after lithiation, and Ni after delithiation, where the charge distributions were described by a Gaussian distribution. After lithiation, the charge of Ni corresponding to  $\text{Ni}^{2+}$  decreases to zero, corresponding to  $\text{Ni}^0$ . After delithiation, the metallic Ni was reoxidized to  $\text{Ni}^{2+}$ .

The Ni–Ni and Ni–O radial distribution functions (RDFs) are shown in *SI Appendix*, Figs. S17 and S18, respectively, and *SI Appendix*, Table S2 summarizes the peak positions and coordination numbers, which are also consistent with the processes of  $\text{Ni}^{2+}$  to  $\text{Ni}^0$  and back to  $\text{Ni}^{2+}$ . At the beginning of the lithiation simulation (NiO), the Ni–Ni RDFs have a strong peak at  $3.075 \text{ \AA}$  corresponding to the nearest Ni–Ni distance in the NiO crystal ( $\text{Ni}^{2+}$ ). After lithiation, the Ni–Ni RDF shifted to  $2.675 \text{ \AA}$ , close to  $2.44 \text{ \AA}$  for metallic Ni. This supports the conclusion that Ni changes from  $\text{Ni}^{2+}$  and  $\text{Ni}^0$  during lithiation. The peak position returns to  $2.975 \text{ \AA}$ , close to the Ni–Ni distance, indicating the process of  $\text{Ni}^0$  to  $\text{Ni}^{2+}$  in delithiation, thus implying that the Ni becomes oxidized again upon delithiation. In addition the coordination number of Ni–O and Li–O shows that the number of oxygen molecules coordinated to Ni decreased from 3.2 to 1.2 during lithiation, whereas the number of oxygen molecules bonded to Li is 1.8. This indicates that during lithiation Li dragged the oxygen out of the NiO crystal, transferring electrons to Ni. After delithiation, the number of oxygens coordinated to Ni increased to 2.6, which is slightly smaller than 3.2. This is because the produced NiO clusters are smaller than the original NiO cap. This is also evidence for the formation of subnanometer-scale NiO clusters on graphene.

To experimentally characterize the mechanism for lithium-induced rescaling, we used XPS and spectroelectrochemical methods under ex situ and in situ. The cell configuration consisted of a Li metal counter/reference electrode and the NiO-n/gr deposited on Au-coated glass as a working electrode. *SI Appendix*, Fig. S20 shows that the Au film is not affected during Li charge–discharge. The cyclic voltammetry (CV) characteristics were obtained for NiO-n/gr at a high scanning rate of  $1 \text{ mV s}^{-1}$  (Fig. 3A). The lithiation resulted in characteristic peaks at about  $0.5 \text{ V}$  (vs.  $\text{Li/Li}^+$ ) for the reaction of  $\text{NiO} + 2\text{Li}^+ + 2\text{e}^- \rightleftharpoons \text{Ni}$ ;  $\text{Li}_2\text{O}$  at the first discharge. Meanwhile, the peaks at around  $1.3$  and  $2.3 \text{ V}$  show that the reverse reaction occurred during delithiation. These peaks indicate the typical characteristics of CV trends for the NiO electrode (16, 17). Also, the graphene-based electrode showed voltage plateaus at around  $0.8 \text{ V}$  for the first discharge, consistent with the well-known reaction of the carbon surface with lithium to form solid electrolyte interface layers (13). The Ni  $2p$  XPS spectra at XPS1 and XPS2 points (Fig. 3A) show that after the discharging (lithiation) process (Fig. 3B) the initial  $\text{Ni}^{2+}$  state shifted to a lower binding energy by  $852.8 \text{ eV}$  for  $2p_{3/2}$  of a  $\text{Ni}^0$  state (18). At the end of the cycle corresponding to the XPS3 point (Fig. 3A), the Ni  $2p$  spectrum shifted back to higher binding energy, indicating that  $\text{Ni}^0$  has returned to  $\text{Ni}^{2+}$ .

We also monitored the electrochemical rescaling process using in situ spectroelectrochemical UV/vis measurements (*SI Appendix*, section S10, Figs. S21 and S22). The points at which the optical spectra were recorded are indicated in Fig. 4A by colored circles. In the first stage of the rescaling process during lithiation,





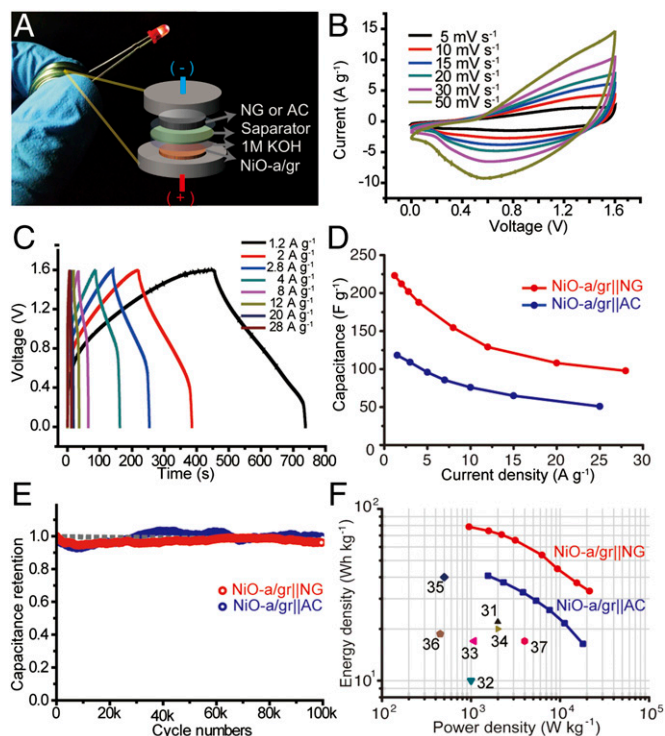


**Fig. 5.** Electrochemical properties of the asymmetric full-cell device. (A) Photograph of a coin-cell-type asymmetric supercapacitor that can store electrical energy to light up an LED. (Inset) Schematic cell configuration of the asymmetric full-cell device using NiO-a/gr and NG electrodes. (B) CV measurements of a two-electrode asymmetric full-cell device at various scan rates. (C) Charge-discharge profiles measured by galvanostatic characterization at various current densities. (D) Gravimetric capacitance of the full-cell configuration based on NiO-a/gr and NG electrodes in addition to that using NiO-a/gr and AC electrodes. (E) Cycling performance of asymmetric full-cell devices based on NiO-a/gr and NG electrodes in addition to that using NiO-a/gr and NG electrodes at a current density of  $12 \text{ A g}^{-1}$ . (F) Ragone plot of capacitors using NiO-a/gr and NG electrodes, NiO-a/gr and AC electrodes, and other data reported in the literature (31–37). All data in this figure are based on the asymmetric capacitor with the total mass of both electrodes.

extremely high compared with those in other morphologies such as NiO nanobelts ( $1,126 \text{ F g}^{-1}$ ) (24), porous NiO on carbon nanotubes ( $1,329 \text{ F g}^{-1}$ ) (25), and NiO/Ni nanocomposites ( $910 \text{ F g}^{-1}$ ) (26). Also, at high current densities of  $33.3$  and  $35 \text{ A g}^{-1}$  for NiO<sub>30</sub>-a/gr, NiO<sub>50</sub>-a/gr, and NiO<sub>70</sub>-a/gr, the capacitances are  $415$ ,  $690$ , and  $1,670 \text{ F g}^{-1}$ , respectively. These values are several times to several hundred times higher than those ( $2$ ,  $9$ , and  $108 \text{ F g}^{-1}$ ) recorded for NiO<sub>30</sub>-n/gr, NiO<sub>50</sub>-n/gr, and NiO<sub>70</sub>-n/gr, respectively. In all cases, the rescaling process dramatically enhanced the pseudocapacitive performance of NiO-n/gr (Fig. 4G). Moreover, the capacitance is maintained for cycling of NiO<sub>50</sub>-a/gr at a current density of  $20 \text{ A g}^{-1}$  for over  $100,000$  cycles (Fig. 4H). The capacitances of NiO<sub>30</sub>-a/gr and NiO<sub>70</sub>-a/gr are similarly preserved during long cycle life (SI Appendix, Figs. S31C and S33C), thus implying that the rescaled particles do not suffer from degradation of the material over time (27, 28). This stability of NiO-a/gr was further validated using an alternative reference electrode (SI Appendix, Fig. S34).

A three-electrode cell was used to determine the available full capacitance for the electrode itself. Meanwhile, the practical device could be fabricated on a two-electrode full cell assembled using positive and negative electrodes. Our earlier report (15) showed that nitrogen-doped graphene is one of the best negative electrodes. In this view, we first fabricated an asymmetric supercapacitor full cell by combining nitrogen-doped graphene

(NG) as a negative electrode while using NiO-a/gr as a positive electrode. We find that this full cell provides sufficient power for operating an LED light (Fig. 5A) and it was operated in a voltage window of  $1.6 \text{ V}$  (Fig. 5B), which was determined through galvanostatic and CV measurements of NG (SI Appendix, Fig. S35) and NiO-a/gr. Fig. 5C shows that the full cell operates at a wide range of current densities ( $1.2$ – $28 \text{ A g}^{-1}$ ). The highest capacitance we observed for the full cell is  $223 \text{ F}$  per  $\text{g}_{\text{NiO-a/gr||NG}}$  at  $1.2 \text{ A g}^{-1}$  (Fig. 5D), where  $\text{g}_{\text{NiO-a/gr||NG}}$  refers to the total mass of negative and positive electrodes. It is notable that the performance of this full cell is limited (29) by the negative electrode with a smaller capacitance of  $285 \text{ F g}_{\text{NG}}^{-1}$  (SI Appendix, Fig. S35). Moreover, we also fabricated an asymmetric full cell using commercial activated carbon (AC) and NiO-a/gr as negative and positive electrodes, respectively (Fig. 5D and SI Appendix, Fig. S36). A capacitance of  $118 \text{ F g}_{\text{NiO-a/gr||AC}}^{-1}$  at  $1.5 \text{ A g}^{-1}$ , close to the ultimate capacitance of AC ( $122 \text{ F g}^{-1}$ ), was obtained. Both full-cell devices present excellent stability with almost  $100\%$  capacity retention over  $100,000$  cycles at a fast current density of  $12 \text{ A g}^{-1}$ , compared with short cycle life using other metal oxide capacitors (30–32). These results suggest that the high-performance pseudocapacitive properties of the NiO-a/gr electrode would allow high capacitance and stable charge retention in a full-cell configuration with other promising counter electrodes.

Moreover, for the full cell using NiO-a/gr and NG electrodes, the highest energy density,  $\sim 80 \text{ Wh kg}^{-1}$  at a power density of about  $1,000 \text{ W kg}^{-1}$ , is achieved while it has the highest power density of  $\sim 21,000 \text{ W kg}^{-1}$  at an energy density of about  $33 \text{ Wh kg}^{-1}$  (Fig. 5F and SI Appendix, section S13). These energy and power densities are excellent compared with those of nickel-oxide-based capacitors (31, 32), nickel-hydroxide-based capacitors (33–35), and manganese-oxide-based asymmetric capacitor devices (36, 37).

## Materials and Methods

**Materials.** All reagents unless otherwise stated were obtained from commercial sources (Sigma-Aldrich and Merck) and were used without purification.

**Lithiation-Induced Rescaling.** First, nickel oxide nanocrystals on graphene were prepared by nickel acetate and graphene oxide (38), as described in SI Appendix, section S1. To synthesize extremely small particles, we used a coin-type cell with Li metal as the counter electrode and with  $1 \text{ M LiPF}_6$  dissolved in a mixture of EC and DEC as the electrolyte ( $1/1 = \text{vol/vol}$ ) for the lithiation-delithiation. NiO on graphene was prepared as a working electrode by mixing with  $10 \text{ wt } \%$  PVDF dispersed in NMP. The black slurry was coated on Cu foil and dried in a vacuum oven at  $80^\circ \text{C}$  overnight. The test cells were assembled with a separator (Celgard) and an electrolyte solution in an Ar-filled glove box. The lithiation-induced rescaling of metal oxides was monitored using a VSP potentiostat (Bio-logic) at a scan rate of  $0.1 \text{ mV s}^{-1}$ . After these processes, the resulting samples were washed with acetone and water to remove residual electrolytes and lithium ions. We then measured the gravimetric mass of the rescaled NiO particles using thermogravimetric and inductively coupled plasma-optical emission spectroscopy analyses.

**Modeling and Simulation.** We started with metallic Li to directly simulate the reaction of  $\text{NiO} + 2\text{Li}^+ + 2\text{e}^- \rightleftharpoons \text{NiLi}_2\text{O}$ . The ReaxFF used in this work combines the Ni–C–H–O force field (39) and Li–C–H–O force field (40) and was optimized to reproduce the conformational energies of Li–O finite molecules and Ni–O finite molecules. We started with a NiO cap on graphene, as shown in SI Appendix, Fig. S13B, for the pure NiO simulations and the same NiO cap with Li atoms added on top, as shown in Fig. 2A, for the lithiation simulations. Three rounds of Li addition were carried out to add a total of  $848 \text{ Li}$  atoms, and each addition was followed by a  $40\text{-ps}$  NVT simulation under an external electronic field of  $0.03 \text{ V nm}^{-1}$  ( $3 \text{ V nm}^{-1}$  for the newly added Li). The NVT molecular dynamics simulation was then extended to  $2 \text{ ns}$  to complete the lithiation. For delithiation, we carried out  $200\text{-ps}$  NVT simulations after removing all of the Li atoms. A time step of  $0.25 \text{ fs}$  was used for all of the simulations. Nosé-Hoover temperature control was used in the NVT simulation at  $300 \text{ K}$  with a damping constant of  $25 \text{ fs}$ .

**Measurement of Surface Faradaic Reactions.** The capacitive performance was measured with a three-electrode device consisting of a platinum wire, a Ag/AgCl electrode (including SCE), and rescaled NiO on graphene, as the counter,

reference, and working electrodes, respectively. The working electrode was prepared by uniformly spreading a slurry composed of the lithiation rescaled sample and a binder (9:1 in mass) on nickel foil and by drying the sample in a vacuum oven at 80 °C. The electrochemical system was assembled with a 1 M KOH aqueous electrolyte and was sealed with Parafilm. The measurements were performed using a Bio-logic VSP potentiostat. The total mass of the composite in the electrode was between 1.3 and 1.5 mg cm<sup>-2</sup>, measured using an XP2U ultramicrobalance ( $d = 0.1 \mu\text{g}$ , Mettler Toledo).

**Full-Cell Type Asymmetric Supercapacitors.** NG electrodes were prepared using the same method as reported in our previous study (15). To investigate the properties of a negative electrode, the as-obtained NG and AC for the negative electrode in a full-cell device were measured under a three-electrode cell configuration of a platinum wire, and a Ag/AgCl electrode in a 1 M KOH.

The CV and galvanostatic measurements were performed using the Bio-Logic VSP potentiostat. The electrochemical properties of the asymmetric full-cell device were investigated under a two-electrode cell configuration. The data analysis of the full-cell device is performed based on the total mass of samples for both electrodes (see *SI Appendix*, section S12 for details).

**ACKNOWLEDGMENTS.** This research was supported by the Global Frontier R&D Program (2013M3A6B1078865) on Center for Hybrid Interface Materials funded by the Ministry of Science, Information and Communication Technology and Future Planning, and the National Research Foundation of Korea (2011-0028737, 2012M1A2A2671813). The work at the Molecular Foundry was supported by the US Department of Energy (DOE) under Contract DE-AC02-05CH11231. D.J.M. was supported by DOE Advanced Research Projects Agency-Energy under the same contract. Support for T.C. and W.A.G. was provided by National Science Foundation (CBET-1067848).

- Dresselhaus MS, Thomas IL (2001) Alternative energy technologies. *Nature* 414(6861):332–337.
- Tarascon JM, Armand M (2001) Issues and challenges facing rechargeable lithium batteries. *Nature* 414(6861):359–367.
- Burke A (2000) Ultracapacitors: Why, how, and where is the technology. *J Power Sources* 91(1):37–50.
- Goodenough JB, Kim Y (2009) Challenges for rechargeable Li batteries. *Chem Mater* 22:587–603.
- Simon P, Gogotsi Y (2008) Materials for electrochemical capacitors. *Nat Mater* 7(11):845–854.
- Kötz R, Carlen M (2000) Principles and applications of electrochemical capacitors. *Electrochim Acta* 45:2483–2498.
- Brezinski T, Wang J, Tolbert SH, Dunn B (2010) Ordered mesoporous alpha-MoO<sub>3</sub> with iso-oriented nanocrystalline walls for thin-film pseudocapacitors. *Nat Mater* 9(2):146–151.
- Reddy RN, Reddy RG (2003) Sol-gel MnO<sub>2</sub> as an electrode material for electrochemical capacitors. *J Power Sources* 124:330–337.
- Chen S, Zhu J, Wu X, Han Q, Wang X (2010) Graphene oxide–MnO<sub>2</sub> nanocomposites for supercapacitors. *ACS Nano* 4(5):2822–2830.
- El-Kady MF, Strong V, Dubin S, Kaner RB (2012) Laser scribing of high-performance and flexible graphene-based electrochemical capacitors. *Science* 335(6074):1326–1330.
- Shipway AN, Katz E, Willner I (2000) Nanoparticle arrays on surfaces for electronic, optical, and sensor applications. *ChemPhysChem* 1(1):18–52.
- Subramanian V, Zhu H, Vajtai R, Ajayan PM, Wei B (2005) Hydrothermal synthesis and pseudocapacitance properties of MnO<sub>2</sub> nanostructures. *J Phys Chem B* 109(43):20207–20214.
- Paek S-M, Yoo E, Honma I (2009) Enhanced cyclic performance and lithium storage capacity of SnO<sub>2</sub>/graphene nanoporous electrodes with three-dimensionally delaminated flexible structure. *Nano Lett* 9(1):72–75.
- Talpin DV, Lee J-S, Kovalenko MV, Shevchenko EV (2010) Prospects of colloidal nanocrystals for electronic and optoelectronic applications. *Chem Rev* 110(1):389–458.
- Jeong HM, et al. (2011) Nitrogen-doped graphene for high-performance ultracapacitors and the importance of nitrogen-doped sites at basal planes. *Nano Lett* 11(6):2472–2477.
- Zhou G, et al. (2012) Oxygen bridges between NiO nanosheets and graphene for improvement of lithium storage. *ACS Nano* 6(4):3214–3223.
- Huang XH, et al. (2009) Morphology effect on the electrochemical performance of NiO films as anodes for lithium ion batteries. *J Power Sources* 188:588–591.
- Mansour AN (1994) Characterization of NiO by XPS. *Surf Sci Spectra* 3:231–238.
- Boschloo G, Hagfeldt A (2001) Spectroelectrochemistry of nanostructured NiO. *J Phys Chem B* 105:3039–3044.
- Nam K-W, et al. (2008) Pseudocapacitive properties of electrochemically prepared nickel oxides on 3-dimensional carbon nanotube film substrates. *J Power Sources* 182:642–652.
- Lee JW, Ahn T, Kim JH, Ko JM, Kim J-D (2011) Nanosheets based mesoporous NiO microspherical structures via facile and template-free method for high performance supercapacitors. *Electrochim Acta* 56:4849–4857.
- Zeng Z, et al. (2011) Single-layer semiconducting nanosheets: High-yield preparation and device fabrication. *Angew Chem Int Ed Engl* 50(47):11093–11097.
- Zeng Z, et al. (2012) An effective method for the fabrication of few-layer-thick inorganic nanosheets. *Angew Chem Int Ed Engl* 51(36):9052–9056.
- Wang B, Chen JS, Wang Z, Madhavi S, Lou XW (2012) Green synthesis of NiO nanobelts with exceptional pseudo-capacitive properties. *Adv Energy Mater* 2:1188–1192.
- Lin P, et al. (2010) The nickel oxide/CNT composites with high capacitance for supercapacitor. *J Electrochem Soc* 157:A818–A823.
- Lu Q, et al. (2011) Supercapacitor electrodes with high-energy and power densities prepared from monolithic NiO/Ni nanocomposites. *Angew Chem Int Ed Engl* 50(30):6847–6850.
- Barani A, et al. (2014) Nanostructured nickel oxide ultrafine nanoparticles: Synthesis, characterization, and supercapacitive behavior. *Mater Sci Semicond Process* 23:85–92.
- Huang ML, Gu CD, Ge X, Wang XL, Tu JP (2014) NiO nanoflakes grown on porous graphene frameworks as advanced electrochemical pseudocapacitor materials. *J Power Sources* 259:98–105.
- Stoller MD, Ruoff RS (2010) Best practice methods for determining an electrode material's performance for ultracapacitors. *Energy Environ. Sci.* 3:1294–1301.
- Yuan C-Z, Gao B, Zhang X-G (2007) Electrochemical capacitance of NiO/Ru<sub>0.35</sub>V<sub>0.65</sub>O<sub>2</sub> asymmetric electrochemical capacitor. *J Power Sources* 173:606–612.
- Wang D-W, Li F, Cheng H-M (2008) Hierarchical porous nickel oxide and carbon as electrode materials for asymmetric supercapacitor. *J Power Sources* 185:1563–1568.
- Luan F, et al. (2013) High energy density asymmetric supercapacitors with a nickel oxide nanoflake cathode and a 3D reduced graphene oxide anode. *Nanoscale* 5(17):7984–7990.
- Li HB, et al. (2013) Amorphous nickel hydroxide nanospheres with ultrahigh capacitance and energy density as electrochemical pseudocapacitor materials. *Nat Commun* 4:1894.
- Yan J, et al. (2012) Advanced asymmetric supercapacitors based on Ni(OH)<sub>2</sub>/graphene and porous graphene electrodes with high energy density. *Adv Funct Mater* 22:2632–2641.
- Tang Z, Tang C-h, Gong H (2012) A high energy density asymmetric supercapacitor from nano-architected Ni(OH)<sub>2</sub>/carbon nanotube electrodes. *Adv Funct Mater* 22:1272–1278.
- Wu Z-S, et al. (2010) High-energy MnO<sub>2</sub> nanowire/graphene and graphene asymmetric electrochemical capacitors. *ACS Nano* 4(10):5835–5842.
- Chou TC, Doong RA, Hu CC, Zhang B, Su DS (2014) Hierarchically porous carbon with manganese oxides as highly efficient electrode for asymmetric supercapacitors. *ChemSusChem* 7(3):841–847.
- Hummers WS, Offeman RE (1958) Preparation of graphitic oxide. *J Am Chem Soc* 80:1339.
- Mueller JE, van Duin ACT, Goddard WA (2010) Competing, coverage-dependent decomposition pathways for C<sub>2</sub>H<sub>2</sub> species on nickel (111). *J Phys Chem C* 114:20028–20041.
- Han SS, van Duin ACT, Goddard WA, 3rd, Lee HM (2005) Optimization and application of lithium parameters for the reactive force field, ReaxFF. *J Phys Chem A* 109(20):4575–4582.